J. Fluid Mech. (2012), *vol.* 695, *pp.* 135–148.
doi:10.1017/jfm.2012.4

Transition to chaos in the wake of a rolling sphere

A. Rao[1]†, P.-Y. Passaggia[2], H. Bolnot[2], M. C. Thompson[1], T. Leweke[2] and K. Hourigan[1,3]

[1] Fluids Laboratory for Aeronautical and Industrial Research (FLAIR), Department of Mechanical and Aerospace Engineering, Monash University, Melbourne, VIC 3800, Australia

[2] Institut de Recherche sur les Phénomènes Hors-Équilibre (IRPHE), CNRS/Aix-Marseille Université, 13384 Marseille CEDEX 13, France

[3] Division of Biological Engineering, Monash University, Melbourne, VIC 3800, Australia

(Received 6 September 2011; revised 18 December 2011; accepted 31 December 2011; first published online 22 February 2012)

The wake of a sphere rolling along a wall at low Reynolds number is investigated numerically and experimentally. Two successive transitions are identified in this flow, as the Reynolds number is increased. The first leads to the periodic shedding of planar symmetric hairpin vortices. The second and previously unknown transition involves a loss of planar symmetry and a low-frequency lateral oscillation of the wake, exhibiting a surprising 7:3 resonance with the hairpin vortex shedding. The two transitions are characterized by dye visualizations and quantitative information obtained from numerical simulations, such as force coefficients and wake frequencies (Strouhal numbers). Both transitions are found to be supercritical. Further increasing the Reynolds number, the flow becomes progressively more disorganized and chaotic. Overall, the transition sequence for the rolling sphere is closer to the one for a non-rotating sphere in a free stream than to that of a non-rotating sphere close to a wall.

Key words: chaos, vortex shedding, wakes

1. Introduction

We here investigate the first transitions in the flow generated by a forward rolling sphere on a solid surface, as the Reynolds number is increased from the initially steady regime. Motivation for this study comes, for example, from the modelling of wall effects in fluid–particle systems, or from biological applications such as cells moving and rolling along blood vessel walls, even though the Reynolds numbers in the latter class are often much lower. Indeed, with rolling near-spherical bodies being ubiquitous in nature (e.g. sand or dust in wind, rocks in avalanches) and in sports (e.g. football, bowls, billiards, pétanque), it seems surprising that the dynamics and transitions of their wakes have been largely unexplored until only recently (Stewart *et al.* 2010*a*).

The case of a non-rotating sphere in a uniform free stream has been studied extensively. This flow undergoes a transition at $Re \simeq 212$ (Johnson & Patel 1999)

† Email address for correspondence: anirudh.rao@monash.edu

from a steady axisymmetric state to a steady non-axisymmetric flow with planar symmetry: the 'double-threaded wake' (Magarvey & Bishop 1961*a*,*b*), consisting of two trailing counter-rotating vortices. Beyond $Re = 272$, these threads interact during formation, leading to the shedding of vortex loops (or 'hairpins'). From analysis of direct simulations, both transitions have been shown to be supercritical (Ghidersa & Dušek 2000; Thompson, Leweke & Provansal 2001*a*), obeying the Landau model as the flow saturates. Numerical simulations indicate that the planar symmetry is broken at $Re \simeq 345$ (Mittal 1999), which is in line with experimental investigations of Sakamoto & Haniu (1990). They suggested that a transitional regime exists for $420 \leqslant Re \leqslant 480$, wherein the hairpin vortices are intermittently displaced to either side of the wake centreline.

Direct numerical simulations were performed by Zeng, Balachander & Fisher (2005) for a sphere moving parallel to a wall. Their study showed that as the sphere was moved closer to the wall, the transition to the unsteady state occurred at Reynolds numbers lower than for the free stream case ($Re < 272$), with a sudden increase observed for the closest tested distance of $0.25D$. The effect of free rotation was also studied. This group (Zeng *et al.* 2009) also performed direct numerical simulations for a stationary spherical particle close to a plane wall in a linear shear flow. They present results for gap ratios between $0.005 \leqslant G/D \leqslant 3.5$, using a symmetry plane. The double-threaded wake is observed at $Re = 200$ for larger gap ratios, while a toroidal structure engulfing the particle is observed for lower Reynolds numbers. These findings are similar to the results of Stewart *et al.* (2010*a*), where the transition to an unsteady state for the non-rotating sphere was in excess of $Re = 300$. Furthermore, they propose empirical relationships for the lift and drag coefficient variation with distance from the wall.

Previous studies by Stewart *et al.* (2010*a*) investigated the wake dynamics of a sphere moving next to a wall, under conditions of forward rolling, sliding or reverse rotation. For the forward-rolling case, which is of interest here, the wake is attached and steady for $Re < 125$. The wake structure shows some similarities to the two-tailed wake of a non-rotating isolated sphere, except that the trailing counter-rotating vortex pair loses strength more quickly with downstream distance due to the damping effect of the wall. Between $125 < Re < 150$, the wake becomes unsteady, periodically shedding vortex loops. The structure is initially symmetric with respect to the vertical plane passing through the sphere and wake. Note that the rotation and the presence of the wall reduces the critical Reynolds number of unsteady flow transition from $Re_c \simeq 212$ (Johnson & Patel 1999; Ghidersa & Dušek 2000; Thompson *et al.* 2001*a*) for the isolated sphere wake. Initial experiments and direct simulations indicated that the wake mirror symmetry is maintained until approximately $Re = 200$, which was the highest Reynolds number reported. Stewart *et al.* (2010*a*) also examined the reverse-rolling case. They observed the development of a transverse sinusoidal oscillation of the wake at $Re = 200$, and recorded a transverse force as the unsteady wake advected downstream. In their simulations at $Re = 300$, initialized from a zero velocity state, it was found that the wake retained mirror symmetry with respect to the wake centreline for a long time. The addition of noise was required to initiate the transition to the asymmetric mode, although this is presumably due to the low growth rate of the instability. The steady double-threaded wake formed downstream of the sphere developed a sinusoidal oscillation, which advected with the flow. Similar sinuous oscillations of the otherwise steady flow were also observed for a translating (sliding) sphere at $Re \geqslant 300$ in the experiments.

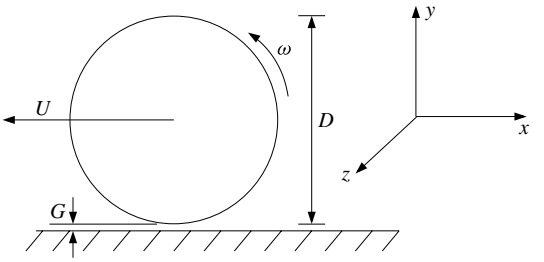

FIGURE 1. Schematic of the configuration. For a forward-rolling sphere, $\omega = 2U/D$.

A first experimental visualization of the transition to an asymmetric rolling sphere wake $Re_c \simeq 200$ was shown in Bolnot *et al.* (2011). The present paper quantifies the transition sequence in this flow determining the critical Reynolds numbers and sub/super-criticality, investigates and characterizes the intriguing high-order resonance between the modes, and quantifies the rapid progression to fully chaotic flow.

2. Problem definition and methodology

A schematic of the rolling sphere setup is shown in figure 1. A dimensionless rotation rate of the sphere, α, can be defined by

$$\alpha = \frac{D\omega}{2U}. \tag{2.1}$$

Here, the sphere diameter is D, the velocity of the sphere centroid is U and ω is the angular velocity. For the situation examined in this paper, α is set to $+1$. This corresponds to prograde non-slip rolling.

For computational efficiency, the reference frame is attached to the centre of the sphere. Relative to this moving frame of reference, the fluid and the lower wall move with the same speed U, directed to the right. The other key governing parameter is the Reynolds number $Re = UD/\nu$, where ν is the kinematic viscosity of the fluid. The force on the sphere consists of viscous and pressure contributions and can be split into streamwise (F_x), vertical (F_y) and lateral (F_z) components. These are non-dimensionalized in the standard way: $C_{x,y,z} = 8F_{x,y,z}/(\rho U^2 \pi D^2)$, with ρ the fluid density. Finally, the non-dimensional shedding frequency is given by the Strouhal number $St = fD/U$, where f is the shedding frequency.

2.1. *Numerical formulation and validation*

The time-dependent incompressible Navier–Stokes equations are solved in cylindrical polar coordinates (r, θ, z). The numerical scheme employs a three-step time-splitting approach (Chorin 1968), with the sub-steps accounting for the advection, diffusion and pressure terms in the Navier–Stokes equations. Previous studies have shown that the implementation achieves second-order temporal accuracy. In terms of spatial discretization, the spectral element method is used for the r–z discretization and a Galerkin Fourier approach for the azimuthal dependence. The method/implementation has previously been used to simulate flows past bluff bodies such as cylinders, spheres and rings both in the free stream (Thompson, Leweke & Williamson 2001*b*; Sheard, Thompson & Hourigan 2003; Schouveiler *et al.* 2004; Ryan, Thompson & Hourigan 2005; Leontini, Thompson & Hourigan 2007) and also close to a surface (Thompson,

Leweke & Hourigan 2007; Stewart *et al.* 2010*b*). Details of the numerical method are provided in Thompson *et al.* (2006).

Because quadrilateral elements are used to build the mesh, the sphere is placed slightly above the wall at a distance G in order to prevent degeneracy of nodes for the elements directly underneath the sphere. A gap ratio of $G/D = 0.005$ is typically used for the simulations. By varying this distance, it was found that the flow structures in the wake were not affected, although the (lift) force on the sphere does vary slightly with increasing gap height (Stewart *et al.* 2010*a*).

The computational domain consisted of 320 macro-elements in the r–z plane. This was extended into three dimensions using N_θ Fourier planes in the azimuthal direction. The origin of the cylindrical polar coordinate system was taken as the point on the wall directly below the sphere with the polar axis passing through the sphere. Each quadrilateral (spectral) element employs $N \times N$ internal node points. These internal node points correspond to the Gauss–Legendre–Lobatto quadrature points with the velocity and pressure fields represented by a tensor product of Lagrangian polynomial interpolants of order $N - 1$ within elements. The macro-elements are concentrated around the sphere and decrease in concentration with increasing distance from it. The top boundary is located $150D$ away from the lower wall while the lateral boundaries are $100D$ away; thus, blockage is negligible. During resolution testing, the interpolant order was varied between $N - 1 = 4$ and 7, with up to 256 Fourier planes. It was found that at $Re = 300$ for $N = 6$ and $N_\theta = 128$, convergence of the drag force is better than 0.5 %, with the Strouhal number resolved to better than 0.1 %.

2.2. *Experimental setup*

Previous experiments by Stewart *et al.* (2010*a*) were undertaken in a closed circuit water tunnel with a moving floor and the sphere mounted on a motor-driven axle parallel to the moving floor. In addition, the upstream boundary layer was sucked off prior to the moving floor section to improve the quality of the entry flow. This setup allowed the sphere to be rotated independently of the wall motion. In the current set of experiments, that extra flexibility was not required and a simpler, less invasive setup was employed. The experimental apparatus consisted of a water-filled tank, with an inclined Plexiglas plate used as a false floor. Steel spheres of diameters 4.7 and 6.5 mm were first coated with fluorescein dye, slowly lowered into the water using a glass pipe and allowed to roll down the incline. The angle between the horizontal and the plate surface was of the order of 0.5° and could be precisely controlled to obtain the desired terminal velocity of the sphere, and hence set the Reynolds number. A 1 mm groove in the inclined surface ensured the sphere rolled along a straight path. The fluid in the tank was illuminated in volume using an argon ion laser, allowing the wake behind the sphere to be visualized and photographed. One distinct advantage of the current setup is the removal of the driven axle, which slightly modifies the flow, and reduced vibration, even though it was necessary to add the groove to ensure passage along a straight path. With the current setup, it was also easy to coat the sphere with dye prior to immersing it and beginning the experimental runs. The velocity of the sphere and thus the Reynolds number was easy to determine accurately from its position in video images.

Various authors (Chhabra & Ferreira 1999; Verekar & Arakeri 2010) have previously studied the distance required to effectively reach the terminal velocity for a sphere rolling down an incline. Chhabra & Ferreira (1999) established an approximate relationship for $Re < 500$ in terms of the density ratio. For the case here using steel spheres, this shows that the terminal velocity is reached within approximately

13 sphere diameters. For the experiments reported in this paper, data were recorded for 120D after the sphere had travelled 30D from its initial position.

3. Results

3.1. *Flow structures*

The flow behind the wake of a rolling sphere has been visualized by Stewart *et al.* (2010*a*), both experimentally by dye visualization in a water channel and also numerically using the method of Jeong & Hussain (1999). In those investigations, steady flow was observed for $Re \leqslant 125$. The visualizations of the flow structures showed the wake is displaced away from the wall at low Reynolds numbers and the formation of a double threaded wake is observed, similar to that behind a non-rotating sphere in unbounded flow for $212 < Re < 272$ (Johnson & Patel 1999). Similar structures were observed in our simulations for $Re \leqslant 135$. However, at $Re = 140$, periodic fluctuations in the time histories were observed for the streamwise and wall normal components of force. The kinking of the double-threaded wake, as described by Magarvey & Bishop (1961*a*,*b*) and Thompson *et al.* (2001*a*), was observed, and hairpin vortices formed behind the sphere advected downstream and moved away from the wall. On further increasing the Reynolds number, the amplitude of the fluctuations increased, while no variation was observed in the lateral component of force, indicating a planar symmetry about the wake centreline. The studies of Stewart *et al.* (2010*a*) show that the symmetry was maintained until $Re = 200$, with the shedding frequency remaining approximately constant at $St \simeq 0.125$ across the unsteady range.

In the current study, numerical simulations at $Re > 195$ showed the growth of the lateral component of the force C_z, whose frequency of oscillation was approximately (but not exactly) twice that of the shedding period for the streamwise direction. The amplitude of the lateral component of force grew with increasing flow speeds beyond $Re = 195$. Tracer particles injected into the flow showed small displacements about the wake centreline at flow speeds near the transition. However, at slightly higher Reynolds numbers, the vortex cores were displaced alternately on either side. The injected dye was drawn into these vortex cores, making it easier to visualize them in the water tank experiments.

Shown in figure 2 are the vortex structures before and after this transition. Figure 2 shows the comparison between the dye visualizations from the experiments (*a*,*b*) and analogous numerical visualizations (*c*,*d*) obtained by injecting tracer particles from a location just above the surface of the sphere. Note that the wake became increasingly chaotic beyond $Re = 220$. This is indicated by the force time traces showing irregular fluctuations, and is discussed in further detail in the following sections.

3.2. *Nature of the transitions*

The Stuart–Landau model for flow supercritical transitions predicts that, close to the critical Reynolds number, the square of the amplitude at saturation should vary linearly with the Reynolds number increment above the critical value (e.g. Provansal, Mathis & Boyer 1987; Dušek, Le Gal & Fraunié 1994; Le Gal, Nadim & Thompson 2001; Thompson & Le Gal 2004). Here, the amplitude can be any flow quantity that is zero prior to transition. For the current flow system, the initial transition is from a steady two-threaded wake to an unsteady wake. In that case, an appropriate measure is the amplitude of the oscillatory component of the drag force coefficient. The second transition corresponds to the breaking of mirror symmetry of the wake as

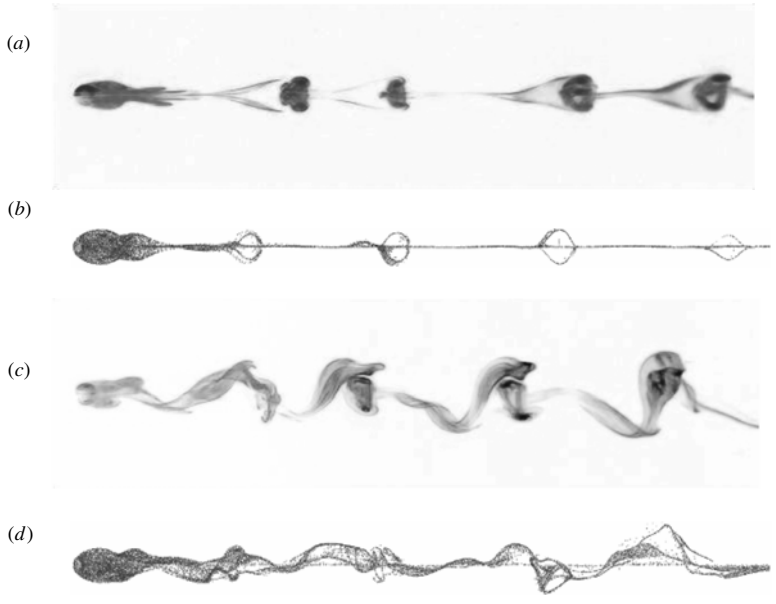

FIGURE 2. Comparison of experimental dye visualizations (*a*,*c*, negative image) and numerically obtained tracer particle images (*b*,*d*). (*a*,*b*) $Re = 190$; (*c*,*d*) $Re = 230$.

viewed from above. In that case, the amplitude of the side force coefficient can be used as a suitable measure. Figure 3 shows plots of the amplitude squared against Reynolds numbers for both transitions determined using data from direct numerical simulations. The unsteady transition occurs at $Re_{c1} = 138.9$ and the mirror symmetry breaking transition occurs at $Re_{c2} = 191.6$. Previously, the critical Reynolds number for the first transition had only been determined to lie in the range $125 < Re_{c1} < 150$, while the second transition was unobserved (Stewart *et al.* 2010*a*). Both plots show that the functional behaviour close to transition is well represented by straight lines, confirming the supercritical (non-hysteretic) nature of both transitions. In terms of the mathematics underlying the Landau model, this means that the real component of the cubic amplitude term in the amplitude evolution equation is negative, meaning that term is responsible for limiting the initial linear growth once the critical Reynolds number is exceeded.

3.3. *Behaviour of the lateral component*

To the knowledge of the authors, the mirror-symmetry breaking transition has not been seen previously in either experiments or numerical simulations. That transition can be further analysed by taking a Fourier transform of the time series of the force coefficients. Power spectra corresponding to the lift and side force components are shown in figure 4 for a range of Reynolds numbers near the lateral transition. At $Re = 200$, just above the transition Reynolds number of $Re = 191.6$, both spectra show peaks at the Strouhal numbers corresponding to the shedding of vortex loops ($St_{x,y} = 0.1167$) and the lateral oscillation ($St_z = 0.05$). These are identified in the spectra. In addition, nonlinear interaction frequency peaks are clearly seen. Some of these have also been marked. As the Reynolds number is increased further to $Re = 240$, the characteristic shedding or lateral oscillation frequency is still present as

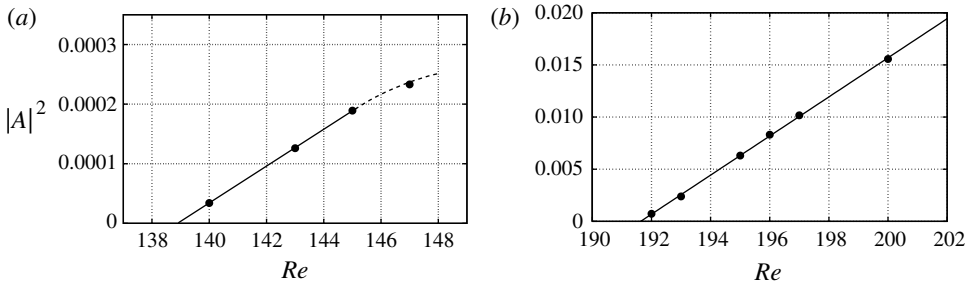

FIGURE 3. Linear fits of the square of the amplitude against *Re* using data obtained from numerical simulations for the first two transitions. The critical values for the transitions are obtained by extrapolating the straight line fits to zero amplitude. See text for further details. (*a*) First transition (steady to unsteady); (*b*) second transition (loss of planar symmetry).

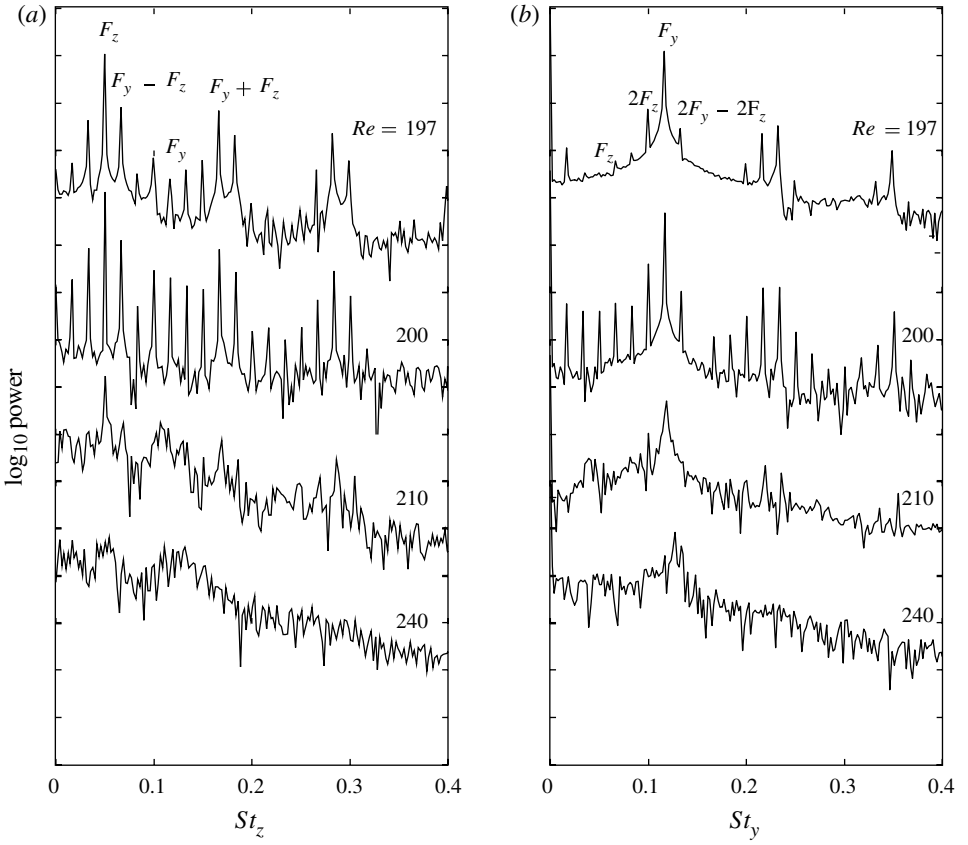

FIGURE 4. Power spectra showing the change in frequency content as a function of Reynolds number. (*a*) The frequency decomposition for the side force (C_z), (*b*) the same for the lift force. Some peaks corresponding to the nonlinear interactions have been labelled.

a broad feature in the C_y and C_z spectra, respectively, but overall the spectra do not show a set discrete set of peaks, indicating a richer frequency content consistent with the evolution towards a chaotic state.

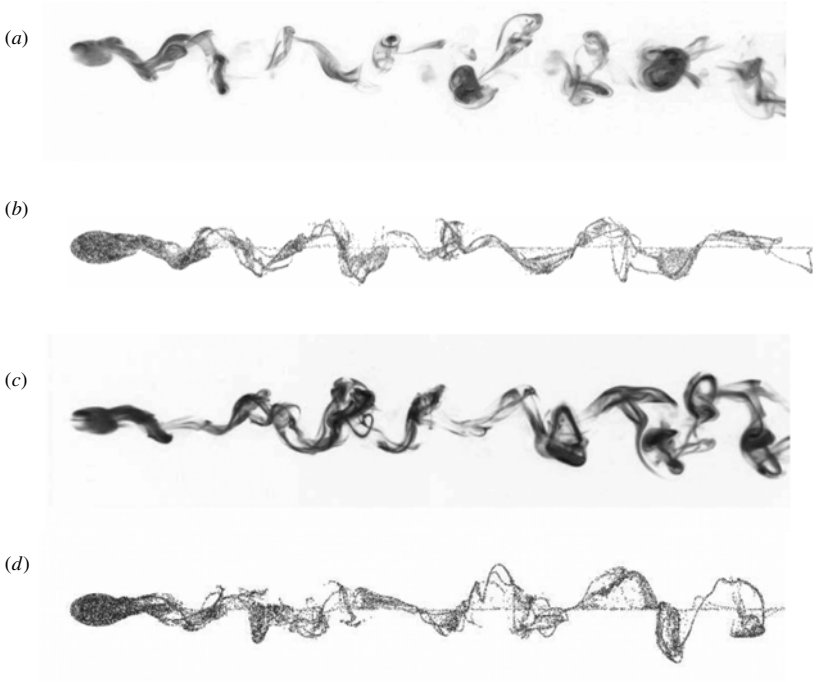

FIGURE 5. Comparison of experimental dye visualizations (*a*,*c*, negative image) and numerically obtained tracer particle images (*b*,*d*), for two higher Reynolds numbers. (*a*,*b*) $Re = 328$; (*c*,*d*) $Re = 415$.

3.4. *Wake behaviour at higher Reynolds number*

Experimental visualizations of the wake show irregular shedding at higher Reynolds numbers. As indicated previously, the wake structures are visualized with dye in the experiments, and for the computations, visualization is undertaken with massless tracer particles originating near the surface of the sphere. Figure 5 shows the visual comparisons in plan view at Reynolds numbers above transition. For the two cases shown, the wakes are clearly asymmetric about the wake centreline and vortex shedding is irregular. The cross-stream extent of the wake increases as the Reynolds number increases. The wake structures obtained appear similar to those in the wake of a non-rotating sphere placed in a free stream at $Re > 650$ (Mittal & Najjar 1993).

3.5. *Force histories*

Sample force histories of the streamwise C_x and lateral C_z components are shown in figure 6 for $Re = 200$ and 300. The lower Reynolds number is just above transition, so the variation of the force components is close to sinusoidal. The C_x component predominantly shows the wake signal corresponding to the formation and shedding of the vortex loops. There is a small degree of modulation due to the cross-stream oscillation. This oscillation in the cross-stream component chiefly corresponds to the post-transition symmetry-breaking sinuous spanwise oscillation, but in turn it is modulated by the vortex-loop formation/shedding signal. At $Re = 200$, the Strouhal numbers of these dominant components are $St_{x,y} = 0.117$ and $St_z = 0.050$.

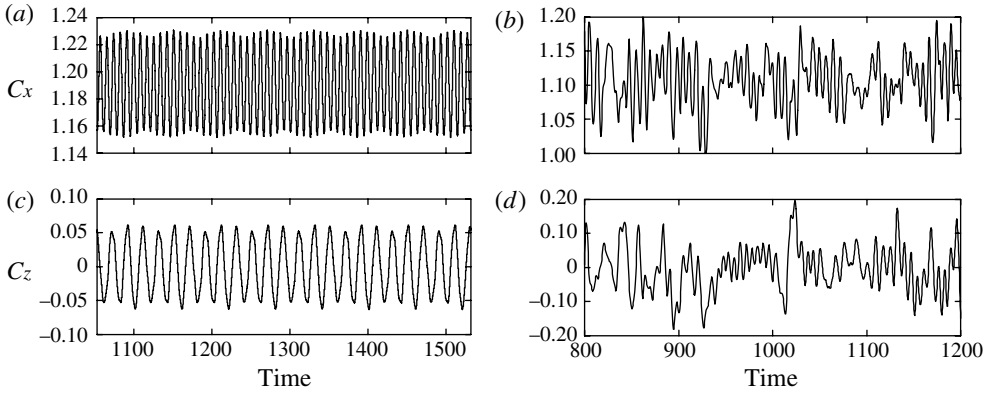

FIGURE 6. Evolution of the drag coefficient C_x (a,b), and the lateral force coefficient C_z (c,d). (a,c) $Re = 200$; (b,d) $Re = 300$.

At the higher Reynolds number of $Re = 300$, the time signals of the force coefficients are very irregular, although the underlying signal corresponding to the shedding of vortex loops is still clearly visible.

Figure 7 shows the variation of the force coefficients with Reynolds numbers. The streamwise component (C_x) decreases, as does the magnitude of the lift coefficient, noting that the force is towards the wall. The lateral component (C_z) fluctuates beyond the transition point. The force coefficients vary smoothly across the transition from the steady to unsteady state. This figure also shows the Strouhal number variation with Reynolds number (7d) corresponding to the drag and lateral force components. After the second transition, there is a sudden shift upwards in the St_x curve. Intriguingly the Strouhal number ratio, St_x/St_z, appears locked to a 7:3 resonance post-transition for $Re_{c2} \leqslant Re \leqslant 205$. This is seen clearly in figure 7(e), which shows this ratio close to the transition. A phase space plot ($C_x(t)$ against $C_y(t-1)$) is displayed in figure 8(a). (Note that the time lag is to make the trajectory more circular so that the individual orbits can be seen more easily.) The boxed region of this subfigure for $Re = 200$ is magnified in figure 8(b). This shows that the trajectory repeats after every 7 orbits for $Re = 200$. Approximately 100 orbits are plotted in this figure. To investigate the apparent resonance further, a simulation was performed at $Re = 215$ with planar symmetry enforced. This gave a Strouhal number consistent with extrapolating the sub-critical St_x curve (see figure 7d), which is quite different to the measured Strouhal number without the restriction. Thus, it does appear that the frequency of the hairpin shedding alters substantially when the lateral oscillation mode is present in order to lock onto the 7:3 resonance. If Re is increased to 220, the phase plot shows that the trajectory is no longer closed with individual orbits broadly following a mean orbit, but with a significant spread. By $Re = 250$, the orbits appear to fill a closed region of phase space, indicating the rapid progression to chaotic behaviour. The broad spectral content at higher frequencies shown in figure 4 supports this conclusion.

A variant of Poincaré surfaces of section was used to investigate this further. These maps are obtained by plotting the streamwise (or lateral) force coefficient against its value one complete lateral (or streamwise) cycle previously, as explained below.

(a) The streamwise and lateral force coefficients were recorded for 400 time units. This corresponds to approximately 20 cycles in the lateral direction and 50 cycles in the streamwise direction.

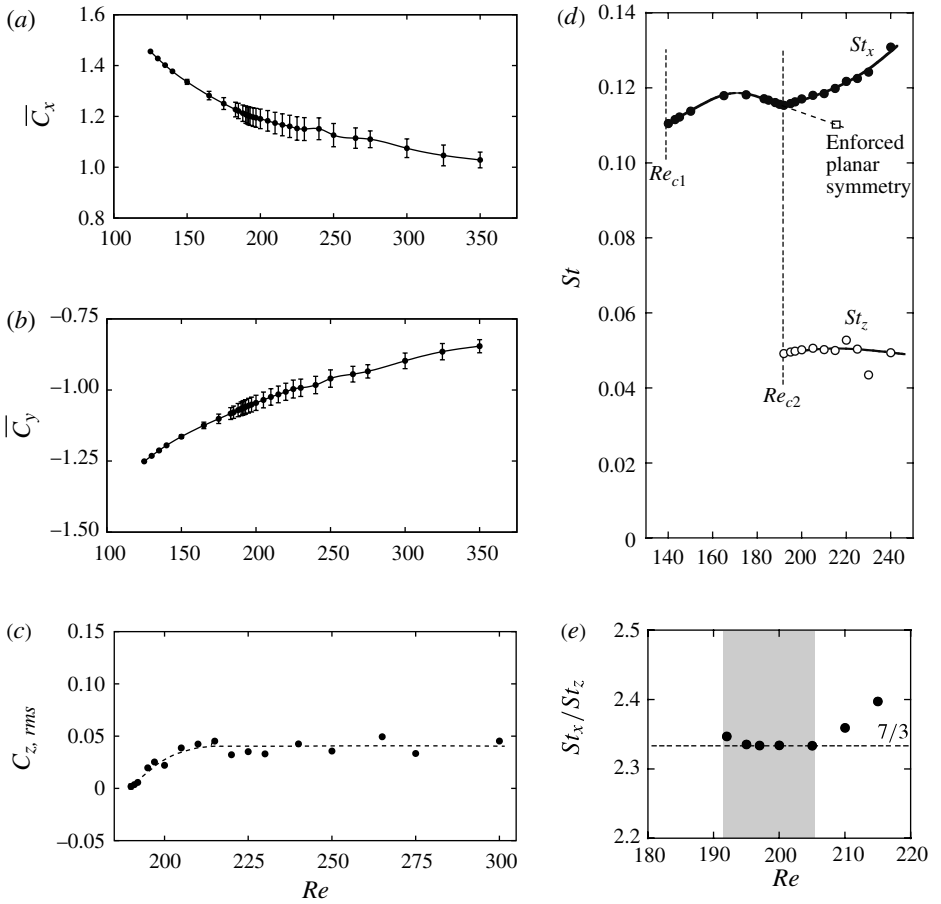

FIGURE 7. Variation of force coefficients and Strouhal numbers with Reynolds number. (*a*) Mean drag coefficient $\overline{C}_x$; (*b*) mean wall-normal force coefficient $\overline{C}_y$; and (*c*) the r.m.s. of the lateral force coefficient $C_{z,rms}$. Error bars represent one standard deviation. (*d*) Strouhal numbers for the drag (St_x) and lateral force (St_z) corresponding to the shedding of hairpin vortices and asymmetric wake oscillations, respectively. (*e*) Strouhal number ratio, St_x/St_z, against Reynolds number near the second critical Reynolds number.

(*b*) The mean value of the coefficient C_x (or C_z) was subtracted from the values of each coefficient.

(*c*) For every complete cycle of C_x (or C_z), the corresponding value of C_z (or C_x) was recorded.

(*d*) $C_{z(n)}$ (or $C_{x(n)}$) was plotted against $C_{z(n-1)}$ (or $C_{x(n-1)}$).

These maps are shown in figure 9. The Poincaré maps are first plotted for $Re = 200$, which is slightly above the critical value of lateral symmetry-breaking transition and in the regime where the flow locks onto the 7:3 resonance. From the two Poincaré maps shown in figure 9(*a*,*b*), we observe that the points lie on a discrete set of fixed points on the surface of section for both the C_x and C_z maps, with the first showing only 3 nodes and the second showing 7 nodes, as required by the 7:3 resonance. These fixed points represent the intersection points of the limit cycle. At $Re = 210$, (figure 9*c*,*d*) the maps show some similarity to those at $Re = 200$, but with the

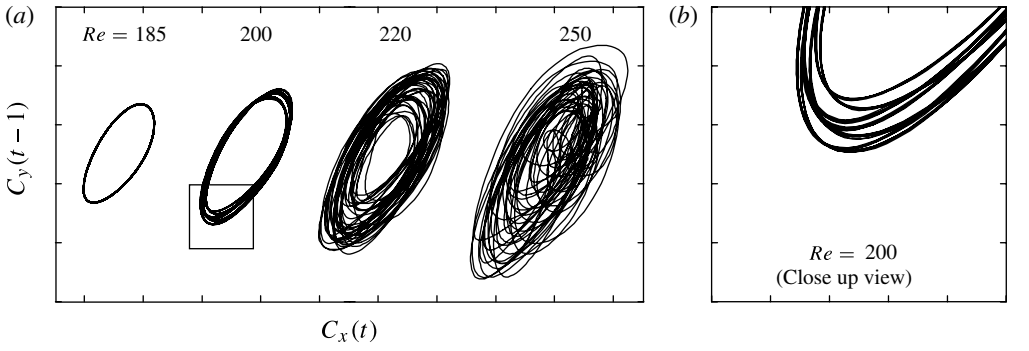

FIGURE 8. (*a*) Qualitative evolution of the phase trajectories of the drag and lift coefficients. Mean values are adjusted, and C_y is plotted with a lag of one time unit for better visual clarity. Tick marks are separated by 0.02 on both axes. (*b*) Close-up of the boxed region for $Re = 200$, showing the trajectory in C_x/C_y space.

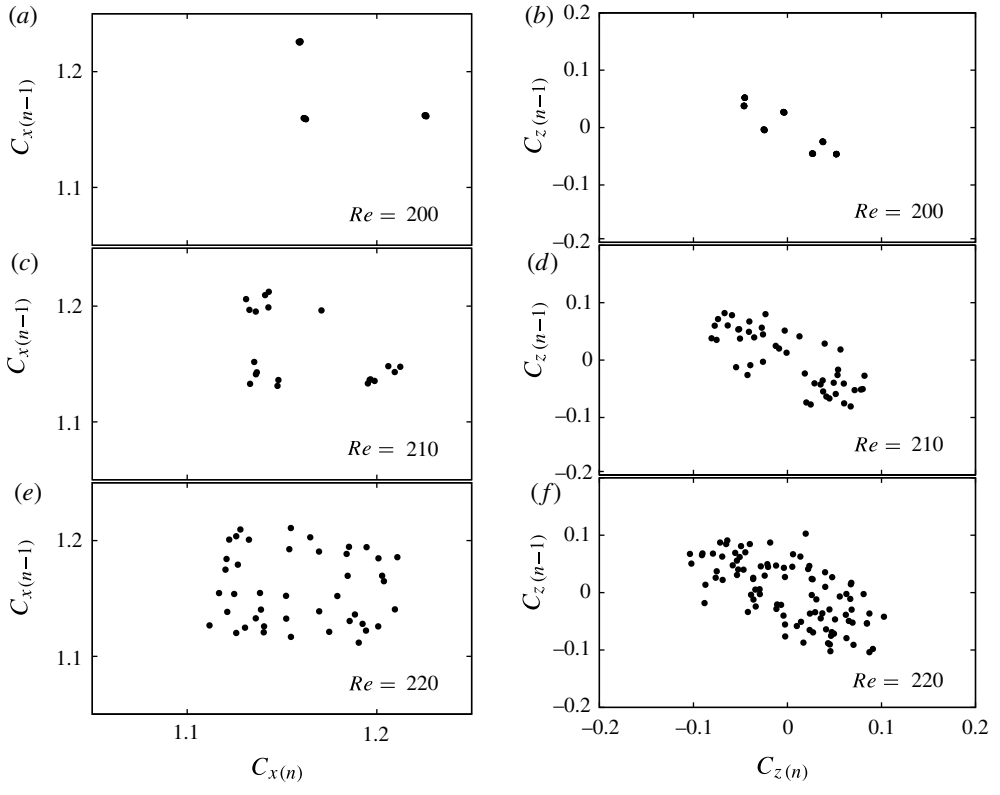

FIGURE 9. 'Poincaré' maps for C_x and C_z, taken for each cycle of C_z and C_x, respectively, at $Re = 200$ (*a*,*b*), 210 (*c*,*d*) and 220 (*e*,*f*).

intersection points instead now clustered around the fixed points. For the C_x map (figure 9*c*) it appears that the points broadly lie in three sets mostly distributed around the three fixed points. While there are insufficient data to be definitive, it appears that this clustering provides evidence of (the disruption of) KAM tori centred on the

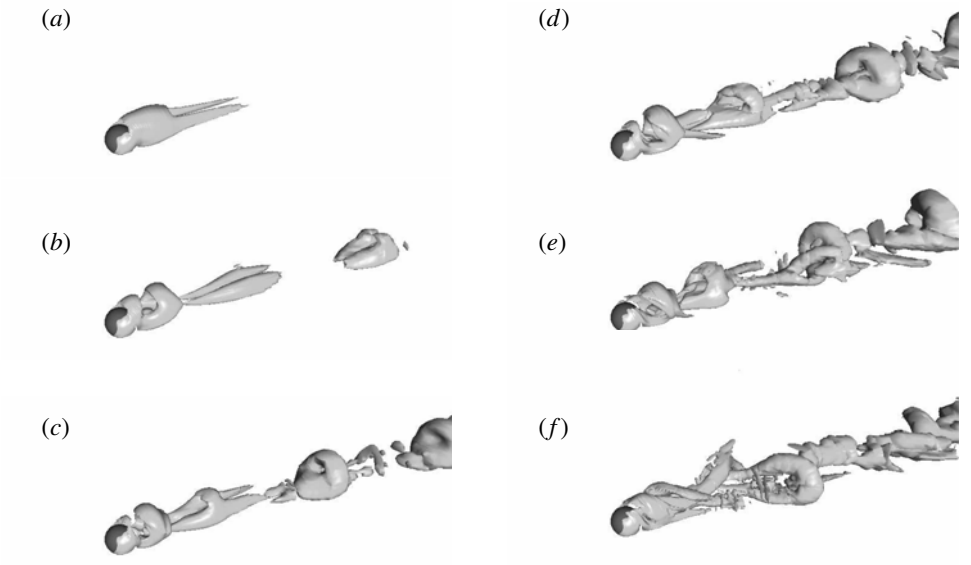

FIGURE 10. Predicted vortical structure of the rolling sphere wake, for increasing Re, visualized using the approach of Jeong & Hussain (1999). The sphere is rolling from right to left. (a) $Re = 125$, (b) $Re = 150$, (c) $Re = 175$, (d) $Re = 200$, (e) $Re = 230$, (f) $Re = 265$.

fixed points, on the route to chaos. This is less clear from the C_z map (figure 9d), although it does appear that the points are not yet space-filling at this stage. A clearer picture might be obtained from longer time series, but the simulation times required are very long. At the higher Reynolds number of $Re = 220$ (figure 9e,f), the Poincaré sections show that the intersection points of the orbits are no longer restricted to lie on or near only fixed points, with the points now appearing randomly distributed over a large region. This shows that the remnants of the 7:3 resonance have disappeared and the governing periods are incommensurate. Together with phase portraits and the frequency spectra, this indicates that the system is undergoing a transition to temporal chaos.

The wake structures in the different flow regimes are summarized in figure 10 for $125 \leqslant Re \leqslant 265$. These images show ($a$) the double-threaded wake, (b) the initiation of unsteadiness, (c) formation of strong vortex loops, (d) breaking of planar symmetry, (e) the development of a lateral oscillation and (f) the progression towards a chaotic wake state.

4. Conclusions

The flow around a rolling sphere has been investigated in detail both numerically and experimentally, including new low background noise level experiments, and a new symmetry breaking transition has been discovered. After the first transition, from a steady to unsteady wake at $Re_{c1} \simeq 139$, the wake remains strictly periodic. Above the second transition at $Re_{c2} \simeq 192$, the two governing frequencies are approximately $St = 0.117$ (for the C_x and the C_y force components) and 0.050 (for the C_z force component). The corresponding oscillations vary in time nearly sinusoidally, each modulated by the other mode, but with these two quite different frequencies. The frequency ratio St_x/St_z appears to lock to 7:3 post-transition up to $Re = 205$, even

though the natural frequencies need to adjust considerably for this resonance to occur. By $Re = 250$, the power spectrum shows broad frequency content, and a plot of C_x versus C_y shows the trajectory starting to fill a closed region of phase space; both are consistent with the rapid progression to chaotic flow.

The wake transition sequence matches that for a non-rotating sphere in a free stream, but not a non-rotating sphere sliding along a wall. In the latter case, the first transition to the double-threaded wake is the sinusoidal cross-oscillation rather than the periodic shedding of loops. For the non-rotating sphere on the wall, fluid can flow freely over the top but not directly underneath. The addition of positive rotation presumably assists the transport of fluid around the underside of the sphere, which counteracts the blockage effect and makes the downstream flow closer to that of an isolated sphere. However, the presence of the wall does reduce the critical Reynolds numbers considerably: from $Re_{c1} = 272$–139 for the unsteady transition, and from $Re_{c2} = 345$–192 for breaking of mirror symmetry. Finally, it is observed that the wake structure shown in figure 10 for $Re = 265$ (and higher) resembles closely that of an isolated non-rotating sphere wake at $Re = 650$ (figure 2*c* of Mittal & Najjar 1993).

Acknowledgements

The authors acknowledge computing-time support from the Victorian Life Sciences Computation Initiative (VLSCI), the National Computational Infrastructure (NCI) and Monash Sungrid. A.R. also acknowledges financial support from the Australian Research Council, under grant no. DP0877328.

REFERENCES

BOLNOT, H., PASSAGGIA, P.-Y., LEWEKE, T. & HOURIGAN, K. 2011 Wake transition of a rolling sphere. *J. Vis.* **14**, 1–2.

CHHABRA, R. P. & FERREIRA, J. M. 1999 An analytical study of the motion of a sphere rolling down a smooth inclined plane in an incompressible Newtonian fluid. *Powder Technol.* **104** (2), 130–138.

CHORIN, A. J. 1968 Numerical solution of the Navier–Stokes equations. *Math. Comput.* **22**, 745–762.

DUŠEK, J., LE GAL, P. & FRAUNIÉ, P. 1994 A numerical and theoretical study of the first Hopf bifurcation in a cylinder wake. *J. Fluid Mech.* **264**, 59–80.

GHIDERSA, B. & DUŠEK, J. 2000 Breaking of axisymmetry and onset of unsteadiness in the wake of a sphere. *J. Fluid Mech.* **423**, 33–69.

JEONG, J. & HUSSAIN, F. 1999 On the identification of a vortex. *J. Fluid Mech.* **285**, 69–94.

JOHNSON, T. A. & PATEL, V. C. 1999 Flow past a sphere up to a Reynolds number of 300. *J. Fluid Mech.* **378**, 19–70.

KARNIADAKIS, G. E. & SHERWIN, S. J. 2005 *Spectral/hp Methods for Computational Fluid Dynamics*. Oxford University Press.

LE GAL, P., NADIM, A. & THOMPSON, M. 2001 Hysteresis in the forced Stuart–Landau equation: application to vortex shedding from an oscillating cylinder. *J. Fluids Struct.* **15**, 445–457.

LEONTINI, J. S., THOMPSON, M. C. & HOURIGAN, K. 2007 Three-dimensional transition in the wake of a transversely oscillating cylinder. *J. Fluid Mech.* **577**, 79–104.

MAGARVEY, R. H. & BISHOP, R. L. 1961*a* Transition ranges for three-dimensional wakes. *Can. J. Phys.* **39**, 1418–1422.

MAGARVEY, R. H. & BISHOP, R. L. 1961*b* Wakes in liquid-liquid systems. *Phys. Fluids* **4**, 800–805.

MITTAL, R. 1999 Planar symmetry in the unsteady wake of a sphere. *AIAA J.* **37**, 388–390.

MITTAL, R. & NAJJAR, F. M. 1993 Vortex dynamics in the sphere wake. *AIAA Paper* 99-3806.

PROVANSAL, M., MATHIS, C. & BOYER, L. 1987 Bénard–von Kármán instability: transient and forced regimes. *J. Fluid Mech.* **182**, 1–22.

RYAN, K., THOMPSON, M. C. & HOURIGAN, K. 2005 Three-dimensional transition in the wake of bluff elongated cylinders. *J. Fluid Mech.* **538**, 1–29.

SAKAMOTO, H. & HANIU, H. 1990 A study of vortex shedding from spheres in a uniform flow. *Trans. ASME: J. Fluids Engng* **112**, 386–392.

SCHOUVEILER, L., BRYDON, A., LEWEKE, T. & THOMPSON, M. C. 2004 Interaction of the wakes of two spheres placed side by side. *Eur. J. Mech.* B **23**, 137–145.

SHEARD, G. J., THOMPSON, M. C. & HOURIGAN, K. 2003 From spheres to circular cylinders: the stability and flow structures of bluff ring wakes. *J. Fluid Mech.* **492**, 147–180.

STEWART, B. E., THOMPSON, M. C., LEWEKE, T. & HOURIGAN, K. 2010*a* Numerical and experimental studies of the rolling sphere wake. *J. Fluid Mech.* **648**, 225–256.

STEWART, B. E., THOMPSON, M. C., LEWEKE, T. & HOURIGAN, K. 2010*b* The wake behind a cylinder rolling on a wall at varying rotation rates. *J. Fluid Mech.* **643**, 137–162.

THOMPSON, M. C., HOURIGAN, K., CHEUNG, A. & LEWEKE, T. 2006 Hydrodynamics of a particle impact on a wall. *Appl. Math. Model.* **30**, 1356–1369.

THOMPSON, M. C. & LE GAL, P. 2004 The Stuart–Landau model applied to wake transition revisited. *Eur. J. Mech.* B **23**, 219–228.

THOMPSON, M. C., LEWEKE, T. & HOURIGAN, K. 2007 Sphere–wall collision: vortex dynamics and stability. *J. Fluid Mech.* **575**, 121–148.

THOMPSON, M. C., LEWEKE, T. & PROVANSAL, M. 2001*a* Kinematics and dynamics of a sphere wake transition. *J. Fluids Struct.* **15**, 575–585.

THOMPSON, M. C., LEWEKE, T. & WILLIAMSON, C. H. K. 2001*b* The physical mechanism of transition in bluff body wakes. *J. Fluids Struct.* **15**, 607–616.

VEREKAR, P. K. & ARAKERI, J. H. 2010 Sphere rolling down an incline submerged in a liquid. In *Proceedings of the 37th International and 4th International Conference on Fluid Mechanics and Fluid Power, 16–18 December, 2010, IIT Madras, Chennai, India*, pp. 1–9.

ZENG, L., BALACHANDER, S. & FISHER, P. 2005 Wall-induced forces on a rigid sphere at finite Reynolds number. *J. Fluid Mech.* **536**, 1–25.

ZENG, L., NAJJAR, F., BALACHANDAR, S. & FISCHER, P. 2009 Forces on a finite-sized particle located close to a wall in a linear shear flow. *Phys. Fluids* **21**, 033302.